How Does Diabatic Heating Affect Tropical Waves Propagation?

Haiyang Yu, Minghua Zhang*

School of Marine and Atmospheric Sciences, Stony Brook University, Stony Brook, New York

September 2017

* Corresponding author address: Minghua Zhang, School of Marine and Atmospheric Sciences, Stony Brook University, Stony Brook, NY 11794-5000

E-mail: minghua.zhang@stonybrook.edu

Abstract

Numerical simulations are performed with a dry dynamical core and idealized physics to study the interactions between different convective heating modes and tropical waves propagation. It is found that the dry adiabatic atmosphere contains abundant tropical wave activities with various spatial and temporal scales. The diabatic convective heating activates particular waves with a scale-selected mechanism, especially the eastward propagating equatorial Kelvin waves with low frequencies and planetary scales. Compared with the deep mode, shallow convective heating favors vertically shorter overturning circulation and slower phase speed, which suggests the importance of the correct simulation of shallow convection in studying tropical waves propagation at the sub-seasonal scale.

1. Introduction

Since the pioneering discovery of the sub-seasonal oscillation in the tropical atmosphere by Madden and Julian [1971], the studies of Madden-Julian Oscillation (MJO), especially on its eastward propagation with a low phase speed (5~10 m s^{-1}) and a period of 30~60 days, have never stopped. In terms of MJO simulation, are we able to reproduce the wave propagations with such low frequencies and planetary scales in the weather or climate models? What are the key processes that account for the eastward propagation of MJO? Such fundamental questions are not well addressed yet, though various theories have been proposed by previous studies, such as the wave conditional instability of the second kind (wave-CISK) mechanism by Lau and Peng [1987], frictional wave-CISK by Wang [1988], wind induced surface heat exchange (WISHE) by Emanuel [1987] and Neelin et al. [1987], convective-radiative feedback by Hu and Randall [1994], moisture mode by Kim et al. [2014], and so on. As an example, a recent study [Jiang et al., 2017] found that the column-integrated horizontal moist entropy advection plays a critical role for the eastward propagation of the MJO in both observation and models, based on the "moisture mode" framework. However, why is the column-integrated horizontal moist entropy advection so important? Which specific physical processes determine the entropy advection? Because the general circulation models (GCMs) include various complex physics, it is difficult to isolate and clarify the physical processes in MJO propagation. Therefore, it would be necessary to use a simplified model and numerical experiments to better understand the detailed mechanisms of tropical waves propagation.

The MJO is associated with two distinguished vertical convective modes: shallow and deep modes, which play different roles in MJO initiation and eastward propagation [e.g. Kiladis et al., 2005]. Based on observation, the MJO convection is found to be generally preceded by low-level convergence and upward motion characterized by shallow convection

as a “precondition”, followed the onset of deep convection [Kiladis et al., 2005]. This shallow-to-deep convection transitions is further found to be sensitive to the midtropospheric moisture buildup and large-scale uplift [Hagos et al., 2014]. Some MJO simulation studies also reported the sensitivities of MJO propagation on the shallow and deep convections. For example, Li et al., [2009] found the MJO propagation characteristics changed dramatically with changing the height of maximum diabatic heating. The bottom heavy heating profile, which may correspond to shallow convection, favored eastward MJO propagation. Zhang and Song [2009] also reported a similar result that a correct simulation of the shallow convection and its interaction with deep convection is the key to the MJO simulation in global climate models. All the previous work suggested the importance of different convective modes in MJO propagation. Therefore, how the shallow and deep convection interact with the large-scale circulation and finally deterimine the tropical waves propogation? We are aiming at address this question by performing numerical experiments with a simplified model and prescribed physics.

2. Model and Experiments

The model used in the present study is a standard Eulerian spectral dynamical core developed using Python language, with the relative vorticity, divergence, temperature, and logarithm of surface pressure as the prognostic variables. The spherical harmonic expanding method with the triangular truncation is used horizontally, and the hybrid coordinate is used in the vertical direction. The model equations are solved with the semi-implicit time-integration method together with Robert filter [Robert et al., 1972]. The detailed description of the spectral dynamical core can been found in Collins et al. [2004], Hoskins and Simmons [1975], and Bourke [1974]. In present study, we perform all the experiments with the same horizontal resolution T30 (about 3.75 degrees) and 18 vertical levels.

In the control experiment, the model starts from a resting atmosphere with the temperature profile at a constant lapse rate (6.5 K km^{-1}) through the troposphere and constant value (217 K) above the tropopause (Figure 1a). Newtonian cooling is implemented continuously to mimic the radiative cooling processes, with the reference temperature the same as the initial condition and a relaxation time of 8 days, while Rayleigh friction is applied with the frictional relaxation time decreasing linearly from 5 days at the surface to zero at 700 hPa (Figure 1b). A locally oscillated diabatic heating center with the period of 44 days is implemented, with a vertical median mode (green line in Figure 1c). The heating is horizontally bell shaped with the dispersion radius of 3000 km zonally and 1500 km meridionally, and centered at the equator (0°N) and dateline (180°E). The control simulation runs for 100 days without any artificial horizontal diffusion, as well as the following experimental runs.

Four restart runs are performed, initialized with the atmospheric status of 44^{th} day of the control run. In the first restart run, as named "no_phy", all the physics are turned off, including the Rayleigh friction, Newtonian cooling, and the diabatic heating. The purpose of this run is to simulate the pure adiabatic processes in the atmosphere. The second "decay" run includes the Rayleigh friction and Newtonian cooling terms, but switches off the implemented diabatic forcing, which will show how tropical wave activities decay with these dynamic and thermodynamic relaxations. In the last two runs: "CISK_deep" and "CISK_shallow", a surface convergence induced diabatic heating scheme is implemented in the model physics to represent the cooperative effect of convective heating and large-scale circulation, which is similar with that in Lau and Peng [1987]:

$$Q_c(p) = \begin{cases} m(p)\dfrac{\min(-D_b, C_{max})}{C_0}, & if\ D_b < 0 \\ 0, & if\ D_b \geq 0 \end{cases} \quad (1)$$

Where, the $m(p)$ is the diabatic heating modes shown in Figure 1c, where the deep mode with the peak at around 380 hPa is used in the "CISK_deep" case and the shallow model with the peak at around 680 hPa is used in the "CISK_shallow" case ; D_b is the wind divergence at the bottom model level (a spherical harmonic spectral filter with the maximum total wave number 3 is performed on the divergence field to maintain numerical stability); $C_{max} = 2 \times 10^{-5}\ s^{-1}$, and $C_0 = 4 \times 10^{-6}\ s^{-1}$. All the settings of these simulations are summarized in the Table 1.

3. Results and Discussions

The time evolutions of surface zonal wind and precipitation from all these five simulations are shown in Figure 2, where the precipitation is diagnosed from vertical integral of diabatic heating profile:

$$P = \frac{c_p}{gL\rho_l}\int_{p_s}^{p_t} Q(p)dp \qquad (2)$$

Where, $Q(p)$ is the diabatic heating profile; p_s is the surface pressure; p_t is the pressure at model top level; c_p is the dry air heat capacity; g is the gravitational acceleration; L is the latent heat of evaporation; ρ_l is the density of liquid water.

In the control run (Figure 2a), a typical Matsuno-Gill mode is generated at the beginning of the simulation, shown as the a westward propagation Rossby wave and a eastward propagation Kelvin wave during the first 10 days. Periodic rainfall and wind pattern are formed associated with locally oscillated heating. Similar to the results by Lau and Peng [1987], the tropical waves induced by the locally oscillated heating show an expanding pattern rather than the westward or eastward propagation. Besides, it should be noticed that there are wind convergence patterns to the east of the heating and precipitation center, implying a vertical westward tilting structure.

When the model is restarted from the 44th day of the control run without any physics (Figure 2b), the tropical waves show strong dispersion as the waves break down into short waves with high frequency, implying that shorter waves have larger growth rates than the longer waves. This phenomenon of wave breaking and dispersion is consistent with the numerical results in Wu [2003], and is well explained by the scale selected mechanism proposed by Wang [1988]. The eastward propagating dry Kelvin waves are found with a phase speed of 43 m s^{-1}, completing one global cycle in about 11 days. When the Rayleigh friction and Newtonian cooling are implemented, the tropical waves dissipate quickly during the first several days (Figure 2c), with just a very small amount of diagnostic precipitation associated with the eastward propagating Kelvin wave.

Once the CISK-like parameterization of convective heating is used, the tropical wave activity will change significantly. In the CISK_deep case (Figure 2d), in which the deep diabatic heating mode is triggered by the surface wind convergence, there is a continuous eastward propagation of wind and rainfall pattern, with the phase speed (30 m s^{-1}; the period is about 15 days) slower than the dry Kelvin waves in the no_phy case. At the beginning of the simulation, weak westward propagating Rossby waves can be found, but dissipate quickly because of less surface convergence. When the shallow diabatic heating mode is used instead of the deep mode, the phase speed of the eastward propagating waves decreases significantly to about 14 m s^{-1} with the period of 32 days, which is closer to the observed period of 30~60 days in MJO. Meanwhile, the precipitation associated with the eastward propagating signal is weaker than that in the deep case, because of the weaker surface convergence induced by the shallow convection. The above differences between the deep and shallow cases strongly support that the well representation of shallow convection is crucial in simulating MJO in general circulation models, as proposed by Zhang and Song [2009].

To get better understanding of the simulation differences, the large-scale vertical circulations of the CISK_deep and CISK_shallow cases at the same model time are shown in Figure 3. The Walker circulations are shown by the zonal mass flux, which is defined as vertical integral of zonal wind anomalies [Hartmann et al., 1984]:

$$M(p) = \frac{1}{g}\int_{p_0}^{p} u^*(p)dp \tag{3}$$

Where, p_0 = 1000hPa; $u^*(p)$ is the zonal wind anomalies derived from the zonal mean zonal wind. As shown in Figure 3, both the deep and shallow diabatic heating modes generate typical Walker circulations, with the narrow rising branchs locating in the heating center and the broad slower subsidence away from the heating. Another similarity is that both cases have a typical baroclinic westward tilting pattern corresponding with the convective heating. As shown in [Kiladis et al., 2005], the surface wind convergence to the east of this vertical tilting pattern supplies moisture to the system and triggers new convection at the leading edge, which determines the eastward propagation. The deep mode produces a deeper (vertical scale is about 8 km) and stronger Walker circulation than that in the shallow case (vertical scale is about 4 km), resulting in a faster eastward propagation of the convection coupled waves. It is consistent with the derivation in Kiladis et al. [2009] that the eastward propagating speed is inversely proportional to the vertical scale of the convection coupled waves.

A more comprehensive way of showing the tropical wave activities is the wavenumber-frequency diagram. As shown in Figure 4, the symmetric spectral power distribution of the surface pressure along the equator from the three cases: no_phy, CISK_deep, and CISK_shallow are shown as the shaded. It is first observed that even in this dry dynamical core without any physics, there are abundant atmospheric internal equatorial wave activities with various wavenumber, frequencies, and equivalent heights, including the equatorial Kelvin waves, Rossby waves, inertial gravity waves. When the CISK-like physics as well as the Rayleigh friction and Newtonian cooling are added, waves with certain

wavenumbers, frequencies and equivalent heights are selectively amplified, especially the eastward propagating Kelvin waves with planetary scales, as shown by the strong signals concentrated in the low frequency regime in Figure 4b and 4c. This is consistent with the scale selection theory derived by Wang (1988) that when boundary layer friction and radiative cooling are considered, the planetary waves are favored to grow rather the short waves that have the largest instabilities in the inviscid situation. Compared with the deep case in Figure 4b, the shallow diabatic heating mode results in shorter equivalent height (Figure 4c) thus smaller eastward propagation speed, as shown by Figure 2e, which is corresponding with a shorter height of the overturning circulation (Figure 3b). This is also consistent with the derivation by Kiladis et al. [2009] that the convection coupled Kelvin wave speed is directly related with the equivalent height, i.e. vertical scale of the convective overturning circulation. Therefore, to get a better simulation of MJO propagation, well representation of shallow convection seems to be necessary and important.

4. Summary

By using a dry dynamical core as well as idealized physics, such as Rayleigh friction, Newtonian cooling, and surface wind convergence induced diabatic heating, we prove that the CISK-like physics is able to mimic the convective coupled equatorial waves with a slower eastward propagation speed than that of the dry equatorial Kelvin waves. More importantly, compared with the deep mode, the diabatic heating mode associated with the shallow convection can generate an eastern propagating convective system with a shallower equivalent depth and slower phase speed, which is closer to the observed behavior of MJO. Therefore, it is suggested that the well representation of shallow convection is crucial in simulating reasonable eastward propagation of the MJO in the weather and climate models.

Though the MJO is largely distinguished from the convection coupled equatorial Kelvin waves, there are some overlaps between them in the wavenumber-frequency diagram. It was shown that the convection coupling waves actually play important roles in MJO propagation, at least in the formation stage of MJO [e.g Hagos et al., 2014]. How do the different diabatic heating modes affect the transition from the initial convection coupled waves to the MJO with the planetary scales? In addition to convective heating, what is the role that radiative forcing plays in eastward propagation? The dynamical core used in the present paper also provides a convenient and feasible platform for studying these scientific questions.

Acknowledgements:

This research is supported by [……]. All the data and codes of the numerical model used in this paper are available upon request from the author (haiyang.yu@stonybrook.edu).

References

Bourke, W. (1974), A Multi-Level Spectral Model. I. Formulation and Hemispheric Integrations. *Mon. Wea. Rev.*, *102*, 687–701.

Collins, W., P. J. Rasch, B. A. Boville, et al. (2004), Description of the NCAR Community Atmosphere Model (CAM 3.0). NCAR Technical Note NCAR/TN-464+STR, DOI: 10.5065/D63N21CH.

Emanuel, K. A. (1987), An air–sea interaction model of intraseasonal oscillations in the Tropics. *J. Atmos. Sci.*, *44*, 2324–2340.

Hartmann, D. L., H. H. Hendon, and R. A. Houze (1984), Some Implications of the Mesoscale Circulations in Tropical Cloud Clusters for Large-Scale Dynamics and Climate. *J. Atmos. Sci.*, *41*, 113–121,

Hoskins, B. J. and A. J., Simmons (1975), A multi-layer spectral model and the semi-implicit method. *Q. J. R. Meteorol. Soc.*, *101*: 637–655.

Hu, Q. and D. A. Randall (1995), Low-Frequency Oscillations In Radiative-Convective Systems. Part II: An Idealized Model. *J. Atmos. Sci.*, *52*, 478–490, doi: 10.1175/1520-0469(1995)052<0478:LFOIRC>2.0.CO;2.

Jiang, X. (2017), Key processes for the eastward propagation of the Madden-Julian Oscillation based on multimodel simulations, *J. Geophys. Res. Atmos.*, *122*, 755–770, doi:10.1002/2016JD025955.

Kiladis, G. N., K. H. Straub, and P. T. Haertel (2005), Zonal and vertical structure of the Madden-Julian oscillation, *J. Atmos. Sci.*, *62*, 2790–2809, doi:10.1175/JAS3520.1.

Kiladis, G. N., M. C. Wheeler, P. T. Haertel, K. H. Straub, and P. E. Roundy (2009), Convectively coupled equatorial waves, *Rev. Geophys.*, *47*, RG2003, doi:10.1029/2008RG000266.

Kim, D., J.-S. Kug, and A. H. Sobel (2014), Propagating vs. Non-propagating Madden-Julian oscillation events. *J. Climate*, *27*, 111-125.

Lau, K., and L. Peng (1987), Origin of low-frequency (intraseasonal) oscillations in the tropical atmosphere. Part I: basic theory. *J. Atmos. Sci.*, *44*:950–972.

Li, C., X. Jia, J. Ling, W. Zhou, and C. Zhang (2009), Sensitivity of MJO simulations to convective heating profiles, *Clim. Dyn.*, *32*, 167–187, doi:10.1007/s00382-008-0455-x.

Madden, R. A. and P. R. Julian (1971), Detection of a 40–50 Day Oscillation in the Zonal Wind in the Tropical Pacific. *J. Atmos. Sci.*, *28*, 702–708.

Neelin, J. D., I. M. Held, and K. H. Cook (1987), Evaporation–wind feedback and low-frequency variability in the tropical atmosphere. *J. Atmos. Sci.*, *44*, 2341–2348.

Robert, A. J., J. Hendersen, C. Turnbull (1972), An implicit time integration scheme for baroclinic models of the atmosphere. *Mon. Wea. Rev.*, *100*, 329 335.

Wang, B. (1988), Dynamics of Tropical Low-Frequency Waves: An Analysis of the Moist Kelvin Wave. *J. Atmos. Sci.*, *45*, 2051–2065.

Wu, Z. (2003), A Shallow CISK, Deep Equilibrium Mechanism for the Interaction between Large-Scale Convection and Large-Scale Circulations in the Tropics. *J. Atmos. Sci.*, *60*, 377–392, doi: 10.1175/1520-0469(2003)060<0377:ASCDEM>2.0.CO;2.

Zhang, G. J., and X. Song (2009), Interaction of deep and shallow convection is key to Madden-Julian Oscillation simulation, *Geophys. Res. Lett.*, *36*, L09708, doi:10.1029/2009GL037340.

Table 1. List of numerical simulations.

Case Name	Initial Condition	Rayleigh Friction	Newtonian Cooling	Diabatic Forcing	Heating Mode
ctrl	Resting atmos.	Yes	Yes	Oscillated	Median
no_phy	44th day of ctrl	No	No	No	--
decay	44th day of ctrl	Yes	Yes	No	--
CISK_deep	44th day of ctrl	Yes	Yes	CISK-like	Deep
CISK_shallow	44th day of ctrl	Yes	Yes	CISK-like	Shallow

Figure Captions

Figure 1. Vertical distribution of (a) initial temperature, (b) Rayleigh friction relaxation time, and (c) different diabatic heating modes.

Figure 2. Hovmöller diagram of zonal wind anomalies at bottom model level (contours with the interval of 1 m s^{-1}; solid and dash contours represent the positive and negative values, respectively) and diagnostic precipitation (shaded, unit: mm day^{-1}) from (a) control run, (b) restart run without any physics, (c) decay case as restart run with Rayleigh friction and Newtonian cooling, (d) restart run with CISK-like deep diabatic heating mode, and (e) restart run with CISK-like shallow diabatic heating mode.

Figure 3. Cross-section of vertical circulation along the equator at the 90^{th} day from (a) CISK_deep and (b) CISK_shallow cases. The zonal mass fluxes are shown as contours with the interval of 2×10^3 kg m^{-1} s^{-1}; negative contours are dashed. Vertical velocities are shaded (unit: 10^{-2} Pa s^{-1}) and scaled with zonal wind anomalies shown as the vectors.

Figure 4. Wave number-frequency power spectrum of the symmetric component of surface pressure (shaded) simulated from (a) no physics run, (b) CISK_deep, and (c) CISK_shallow cases. Dispersion curves for the Kelvin wave (blue solid lines), n=1 equatorial Rossy wave (green solid lines), and n=1 inertio-gravity wave (red solid lines) are plotted for equivalent depths of 5, 20, 50 m. Periods (unit: day) are shown on the labels of vertical axis.

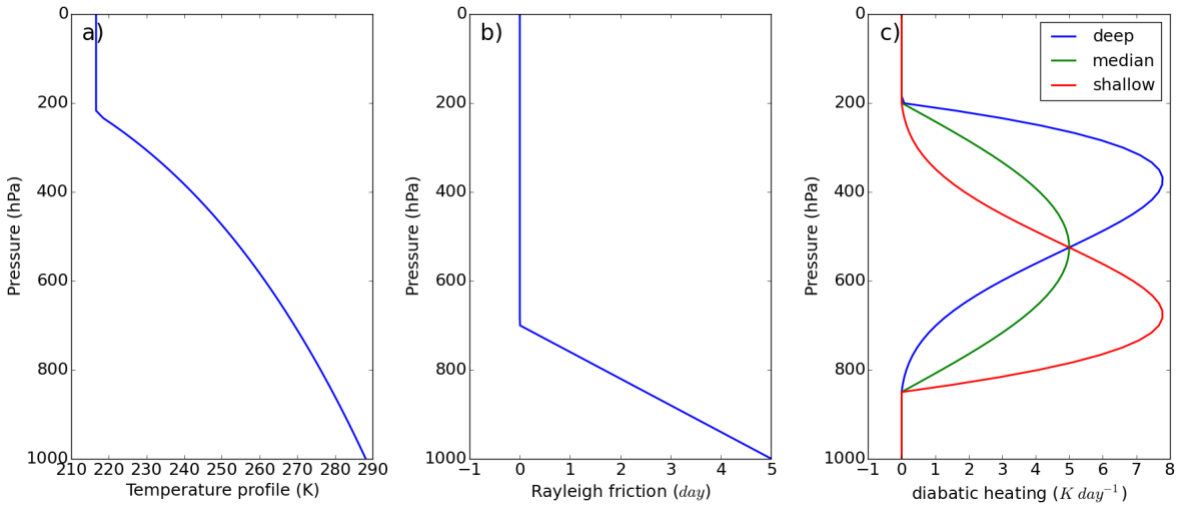

281

282 **Figure 1.** Vertical distribution of (a) initial temperature, (b) Rayleigh friction relaxation

283 time, and (c) different diabatic heating modes.

284

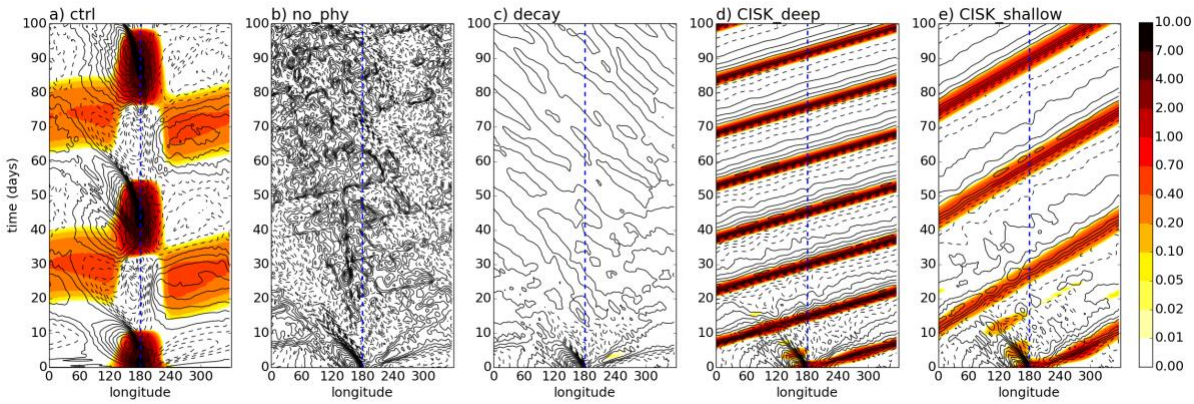

285

286 **Figure 2.** Hovmöller diagram of zonal wind anomalies at bottom model level (contours with
287 the interval of 1 m s^{-1}; solid and dash contours represent the positive and negative values,
288 respectively) and diagnostic precipitation (shaded, unit: mm day^{-1}) from (a) control run, (b)
289 restart run without any physics, (c) decay case as restart run with Rayleigh friction and
290 Newtonian cooling, (d) restart run with CISK-like deep diabatic heating mode, and (e) restart
291 run with CISK-like shallow diabatic heating mode.

292

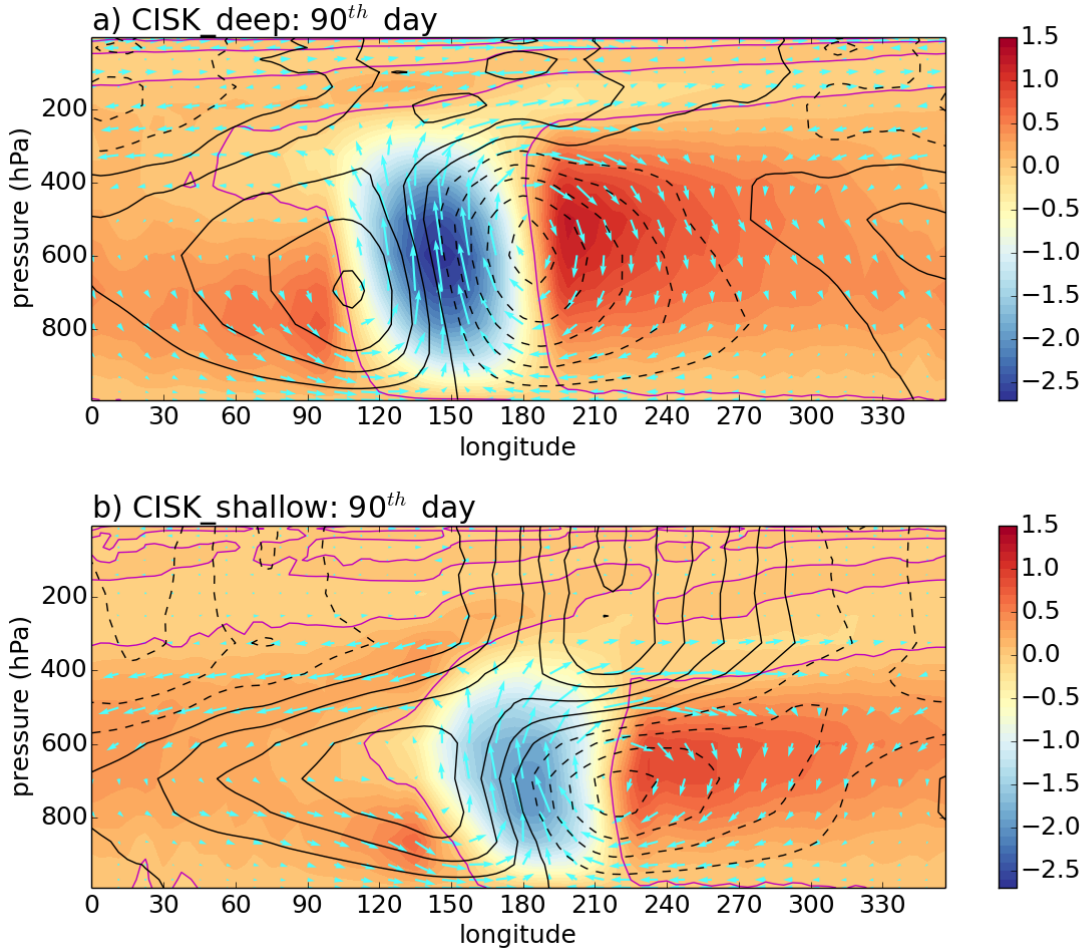

293

294 **Figure 3.** Cross-section of vertical circulation along the equator at the 90th day from (a)

295 CISK_deep and (b) CISK_shallow cases. The zonal mass fluxes are shown as contours with

296 the interval of 2×10^3 kg m^{-1} s^{-1}; negative contours are dashed. Vertical velocities are shaded

297 (unit: 10^{-2} Pa s^{-1}) and scaled with zonal wind anomalies shown as the vectors.

298

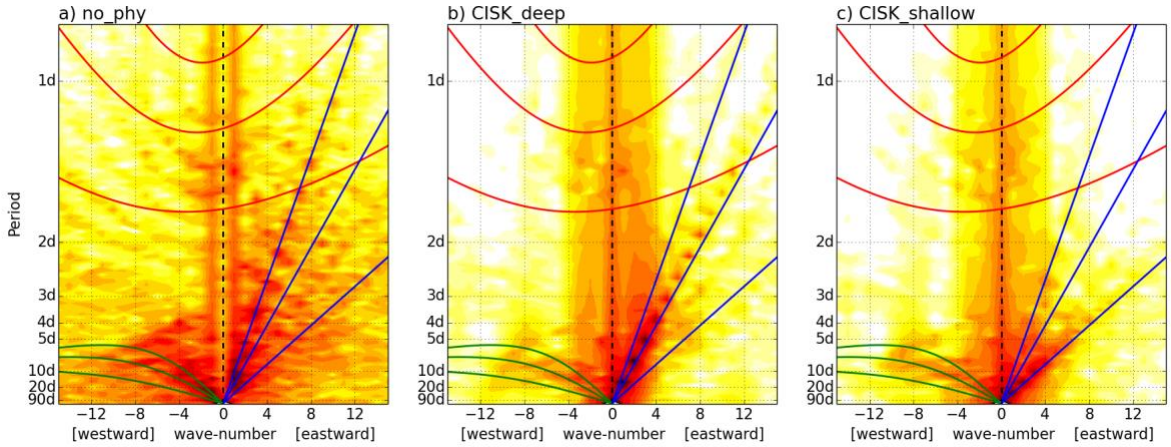

299

300 **Figure 4.** Wave number-frequency power spectrum of the symmetric component of surface
301 pressure (shaded) simulated from (a) no physics run, (b) CISK_deep, and (c) CISK_shallow
302 cases. Dispersion curves for the Kelvin wave (blue solid lines), n=1 equatorial Rossy wave
303 (green solid lines), and n=1 inertio-gravity wave (red solid lines) are plotted for equivalent
304 depths of 5, 20, 50 m. Periods (unit: day) are shown on the labels of vertical axis.